

– 1 –

The optical - ultraviolet continuum of Seyfert 2 galaxies

M. Contini¹ and S.M. Viegas²

¹ School of Physics and Astronomy, Tel-Aviv University, Ramat-Aviv, Tel-Aviv, 69978, Israel

² Instituto Astronômico e Geofísico, USP, Av. Miguel Stefano, 4200,04301-904 São Paulo, Brazil

Running title : The continuum of Seyfert 2 galaxies

subject headings : galaxies : Seyfert - galaxies: - continuum - galaxies: shock waves - ultraviolet: galaxies

Abstract

This paper aims to understand the continuum of Seyfert 2 galaxies. By fitting the single galaxies in the sample of Heckman et al. (1995) with composite models (shock+ photoionization), we show that five main components characterize the SED of the continuum. Emission in the radio range can be recognized as bremsstrahlung from relatively cold gas, or synchrotron radiation due to Fermi mechanism at the shock front. The bump in the IR is due to reradiation of the central radiation by dust and to mutual heating and cooling between dust and gas. In the optical-UV range the main component is due to bremsstrahlung from gas heated and ionized by the primary flux (the flux from the active center (AC) or/and the radiation from young stars), by diffuse radiation emitted by the hot slabs of gas, and by collisional ionization. Shocks play an important role since they produce a high temperature zone where soft X-rays are emitted. Finally, the harder X-ray radiation from the AC, seen through the clouds, is easily recognizable in the spectrum. Assuming that the NLR is powered by a power-law central ionizing radiation and by shocks, we discuss the optical-ultraviolet featureless continuum of Seyfert 2. We show that in this wavelength range, the slope of the NLR emission reproduces the observed values, and may be the main component of the featureless continuum. However, the presence of star forming regions cannot be excluded in the circumnuclear region of various Seyfert galaxies. Their photoionizing radiation may prevail in the outskirts of the galaxy where the power-law radiation from the AC is diluted. An attempt is made to find their fingerprints in the observed AGN spectra. Finally, it is demonstrated that multi-cloud models are necessary to interpret the spectra of single objects, even in the global investigation of a sample of galaxies.

1. Introduction

Observational data in the ultraviolet range are now available for more and more galaxies. They complete the range of the observed frequencies and permit a better interpretation of the emitted spectra. The nature of the ultraviolet continuum in type 2 Seyfert galaxies was investigated by Heckman et al. (1995) on the basis of the IUE spectra of 20 galaxies (hereinafter, this sample is referred to as HS). Various possibilities were considered to explain the observed featureless continuum, as, for example, light from a hidden Seyfert 1 nucleus scattered by dust or warm electrons. The results show that no more than 20 % of the Seyfert 2 template's continuum can be light from a hidden Seyfert 1 nucleus. The alternative favored by Heckman et al. is that most of the UV continuum in these galaxies is produced by a reddened circumnuclear starburst. Heckman et al. claim that the UV spectral slopes and the ratios of far IR to UV continuum fluxes are very similar to the corresponding properties of typical metal-rich, dusty starburst galaxies.

The interpretation of the observed continuum (and line) spectra of the galaxies is difficult due to the complex structure of the emitting regions. Modeling is crucial to disentangle the different components contributing to a single galaxy spectrum.

Previous papers on active galactic nuclei (AGN) and starburst galaxy emission spectra (Contini, Prieto, & Viegas 1998a,b, Viegas, Contini, & Contini 1999, Contini et al 1999) have shown that multi-cloud models are necessary to fit the observational data even in a single region of a galaxy. Moreover, the spectral energy distribution (SED) of AGN and starburst galaxy continua can be roughly decomposed into five components. Emission in the radio range can be recognized as bremsstrahlung from relatively cold gas, or synchrotron radiation due to the Fermi mechanism at the shock front. The bump in the IR is due to reradiation by dust of the central radiation. In the optical-UV range the main component is due to bremsstrahlung from the clouds photoionized by the flux from the active center (AC) and the radiation from young stars, by diffuse radiation emitted by the hot slabs of gas, as well as by collisional ionization. The shock plays an important role since it produces a high temperature zone emitting soft X-rays. Finally, the hard X-ray radiation from the AC, seen through the clouds or through the dust torus, is easily recognizable in the spectrum. Previous results (Contini, Prieto & Viegas 1998a,b) show that the SED of the continuum in the various frequency ranges are often correlated.

In order to further investigate the nature of the continuum of HS galaxies, we have simulated the galaxy spectra by multi-cloud composite models. These models account for the photoionizing effect of the radiation from the AC source, as well as for shock effects on the emitting clouds.

One of our goals is to search for starburst or AGN characteristics prevailing in single objects and see how these can be recognized by the analysis of the spectra. Actually, we focus on the continuum, looking for the features that are easily recognized in the observed spectra. We show that for consistency, however, both the continuum and line spectra must be considered. The physical conditions in single galaxies and in the whole sample are also investigated. Another goal is to verify if the continuum obtained from the components listed above reproduces the observed characteristics of the HS galaxies, in particular the slopes discussed by Tran (1995) and by Heckman et al. (1995).

For all the objects of the sample, the fit of the observed continuum SED and the main characteristics of the models explaining the observed continuum are presented in §2. The line ratios are presented and discussed in §3. Concluding remarks follow in §4.

2. The SED of the continuum

We consider composite models for the NLR which account consistently for the effects of an ionizing radiation flux from an external source and of the shocks due to cloud motions. The SUMA code (see, for instance, Viegas & Contini 1994) is used.

The input parameters are the shock velocity, V_s , the preshock density, n_0 , the preshock magnetic field, B_0 , the ionizing radiation spectrum, the chemical abundances, the dust-to-gas ratio by number, d/g , and the geometrical thickness of the clouds, D . A power-law, characterized by the power index α and the flux, F_H , at the Lyman limit, reaching the cloud (in units of $\text{cm}^{-2} \text{s}^{-1} \text{eV}^{-1}$) is generally adopted. However, for some models a high temperature ($T_* = 1-2 \times 10^5 \text{ K}$) blackbody ionizing radiation is used, characterized by the ionization parameter U . This high blackbody temperature could be associated to an evolved stellar cluster (Terlevich & Melnick 1985, Cid-Fernandes, Dottori, Gruenwald & Viegas 1991). Some models with a blackbody spectrum at lower temperature ($T_* = 5 \times 10^4 \text{ K}$) are also considered, in order to mimic ionization by a starburst.

For all the models, $B_0 = 10^{-4} \text{ gauss}$, $\alpha = 1.5$, and cosmic abundances (Allen 1973) are adopted. The remaining input parameters are listed in Table 1. Notice that some of the models differ only in the dust-to-gas ratio. SUMA accounts for silicate grains with an initial radius of $0.2 \mu\text{m}$. The grains are sputtered entering the shock front (see Viegas & Contini 1994). The d/g ratio by mass in the Galaxy is $\sim 4.1 \times 10^{-4}$ (Drain & Lee 1994) which corresponds to $d/g \sim 10^{-14}$ by number, adopting a silicate density of $\sim 3 \text{ g cm}^{-3}$.

Previous results, obtained by self-consistently fitting the continuum and emission-line spectra of the Circinus galaxy and NGC 5252, confirm that velocities of $100\text{-}1000\text{ km s}^{-1}$ are present in the narrow line region of Seyfert 2 galaxies, with preshock densities of $100\text{-}1000\text{ cm}^{-3}$. The ionizing flux from the AC are about $10^{11} - 10^{12}\text{ photons cm}^{-2}\text{ s}^{-1}\text{ eV}^{-1}$ at 1 Ryd.

2.1. Theoretical results : the optical-UV peak

The calculated optical-ultraviolet continuum depends on the temperature distribution across the emitting clouds. An illustration of the results is presented in Figure 1. The most significant models are chosen with the following criteria: shock velocities in the range $100\text{-}300\text{ km s}^{-1}$, characterizing the velocity field of the NLR, with related pre-shock densities in the range $100\text{-}300\text{ cm}^{-3}$, in order to reproduce the observed densities. Such V_s values produce postshock zones with temperatures of about $\sim 10^5 - 10^6\text{ K}$. Regarding the ionizing radiation, the characteristic $\log F_H$ generally varies between 10 and 12.7.

Assuming that starbursts can also be effective in AGN, we present the results of models with a black body temperature of $5\text{ }10^4\text{ K}$ which are in agreement with starburst values and U between 0.01 and 1 (see Viegas et al. 1999).

The results are shown in Figure 1a for a power-law radiation and in Figure 1b for the $T_* = 5\text{ }10^4\text{ K}$ blackbody radiation, with dust-to-gas ratio equal to 10^{-15} . In each figure, the left pannel shows the temperature distribution across a cloud, where the left edge of the diagram corresponds to the shock front, while the right edge to the photoionized side. The right pannel shows the corresponding SEDs.

The particular case of a blackbody spectrum with a high ionization parameter ($U=100.$, Table 1b, left pannel) shows that black body radiation hardly heats the gas to temperatures higher than $T = 10^4\text{ K}$, since there are not enough high energy photons. On the other hand, for power-law models higher gas temperatures ($T \simeq 4 \times 10^4\text{ K}$) can be reached depending on F_H .

The peak of bremsstrahlung emission in the optical range of the SED depends on the temperature distribution across the clouds. Therefore, different sets of input parameters provides SEDs with different shapes. The peaks, shown in Figures 1a and 1b, correspond to gas at $\simeq 10^4\text{ K}$, while the peaks in the soft X-rays are produced by the gas at higher temperatures in the post-shock region, and are clearly related to the shock velocity.

2.2. Comparison with the observations

In Figure 2 the spectral luminosities of all the galaxies of the sample (open squares) appear together. NGC 3393 is recognizable as the lower limit (crosses) and NGC 7582 as the upper limit (open triangles).

The references of the observational data for the continuum of the Seyfert 2 galaxies of HS, from infrared to X-rays appear in Table 2a. The 1.4 GHz data were taken from Heckman et al. (1995).

A roughly common shape of the SED can be noticed. In the radio range the data show the band of the luminosities. Collectively, however, they cannot indicate any kind of slope, either with bremsstrahlung or with power-law characteristics (Fermi mechanism).

On the basis of the previous analysis of the continuum and emission line spectra of individual Seyfert 2 galaxies, we have selected the least number of models which fit the continuum of the HS galaxies (see Table 1). The great number of different conditions obtained by the full modeling of individual objects shows that modeling a sample collectively can give only a rough idea of the real picture.

2.2.1. Fitting the continuum : the sample

The observed and calculated continuum SEDs are compared in Figure 3. The SED of the continuum in the optical-UV range shows a complex nature. Notice that the data are, generally, not reddening corrected, however, the correction is small, even in the optical-UV range with $E(B-V)$ between ~ 0.0 and 0.1 ($E(B-V) \simeq 0.35$ for NGC 2110, McAlary et al 1983).

One of the difficulties of the study of the AGN continuum is the extraction of the stellar population component. Extraction of the stellar continuum from long slit spectroscopic data of AGN are usually obtained using a template (see, for instance, a comprehensive analysis by Cid-Fernandes, Storchi-Bergmann & Schmitt 1998). For low dispersion data as used in this paper, however, a less sophisticated correction is usually applied; the stellar continuum is represented by a low temperature blackbody component. Here, for all the galaxies, a blackbody spectra with $3 \cdot 10^3 \text{ K} \leq T \leq 5 \cdot 10^3 \text{ K}$ is used to mimic the emission from the old-stellar galactic population which contributes to the nuclear continuum. Model results are then used to fit data, in the same frequency range, that are uncontaminated by the old stellar population. These results correspond

mainly to bremsstrahlung from gas photoionized by the AC radiation. The diffuse secondary emission from the hot slabs of the shocked gas may also contribute to the optical-ultraviolet spectrum.

For each galaxy the models representing the main components are given in Table 2b. The black body temperature corresponding to the old population stars is given in column 2 and the input parameters of the models in columns 3-7. In column 8 we give the weights (W) which are adopted to fit the data for each model. They represent the ratio of the emitting surface at the nebula to the surface at earth ($4\pi d^2$, where d is the distance to the galaxy). The covering factor (η) - corresponding to the models fitting the SED between 10^{14} - $5 \cdot 10^{14}$ Hz - is calculated assuming that the NLR is located ~ 1 Kpc from the central source and is listed in column 9. Notice that the models which fit the SED at 10^{14} - $5 \cdot 10^{14}$ Hz generally show the highest η , thus the values listed in Table 2b are upper limits.

Regarding the galaxies in the sample, Figure 3 shows that:

- 1) For most of the galaxies, the data available in the radio range are not sufficient to indicate a definitive slope characterizing the emission mechanism. However, for NGC 2992, Mrk 3, and Mrk 463 the radio emission corresponds to synchrotron radiation produced by the Fermi mechanism at the shock front (Contini, Prieto, & Viegas 1998b). On the other hand, for NGC 2110, NGC 3393, NGC 4388, NGC 5135, NGC 5643, NGC 6221, NGC 7582, and Mrk 348 the radio emission is dominated by free-free radiation that can often be reduced by absorption.
- 2) Emission in the IR is due to reradiation by dust (see Kraemer & Harrington 1986). Generally, the observational data are better explained by a multi-cloud model (e.g. NGC 3393, NGC 4388). In these cases, the dust temperature is different in the different clouds and each component peaks at a different frequency. Thus, the resulting peak is flatter, better reproducing the observed data. For NGC 2110, NGC 3393, NGC 5506, Mrk 3, Mrk 34, Mrk 78, Mrk 348, IC 3639, and IC 5135 the dust-to-gas ratio in some of the clouds is particularly high ($\sim 10^{-13}$).
- 3) Except for Mrk 477 and Mrk 573, an old stellar population, with temperatures in the range 3 to $5 \cdot 10^3$ K, seems to be contributing to the optical continuum of the galaxies in the sample, representing the underlying stellar population.
- 4) Soft X-ray data are fitted by gas with a high shock velocity ($> 900 \text{ km s}^{-1}$). This soft-X ray component originates from the post-shock zone where $V_s \sim 900 \text{ km s}^{-1}$, corresponding to temperatures of $\sim 1.2 \cdot 10^7$ K. Such temperatures are in good agreement with the Raymond-Smith

interpretation of the ASCA soft X-rays data for NGC 5506 (Wang et al. 1999) and NGC 7582 (Xue et al. 1998) which gives $T \sim 10^7$ K. Also for NGC 2110 temperatures of $6.8 \cdot 10^6$ - $1.5 \cdot 10^7$ K are deduced from ROSAT soft X-ray data (Weaver et al 1995).

Dust grains can also be heated to relatively high temperatures (Viegas & Contini 1994) in the post shock region. Consequently, besides the soft X-ray emission, the shape of the mid-IR continuum may provide another key to the presence of high velocity clouds in AGN. In this case we expect the mid-infrared emission to be correlated with the soft X-ray component. For the galaxies analysed here, high velocity clouds ($V_s = 900\text{-}1000 \text{ km s}^{-1}$) invoked to explain the data in the soft X-ray and in the near IR generally have *normal* dust-to-gas ratios ($10^{-13} - 10^{-15}$).

5) The d/g ranges from $5 \cdot 10^{-16}$, in poor dusty cases, to $> 10^{-13}$, in dusty clouds (Table 1). Very different conditions can be found in different clouds of the same galaxy (e.g Mrk 477) . In fact, dust, which is generally present in star forming regions, can be destroyed by sputtering and evaporation. Therefore, the effect of the shock is crucial because sputtering and evaporation depend on the shock velocity and on the grain temperature, respectively.

Finally, Fig. 3 shows that shock velocities of $\sim 200 \text{ km s}^{-1}$ and preshock densities of $\sim 200 \text{ cm}^{-3}$ strongly prevail in the fit of the data in the optical range. On the other hand, the data in the optical-UV range, between 4250 \AA and 1200 \AA (corresponding to $\log \nu = 14.85 - 15.4$), are better fitted by model 1, characterized by $V_s = 100 \text{ km s}^{-1}$ and a relatively high F_H .

2.2.2. Fitting the continuum : particular models

Starbursts in the circumnuclear region

The fit of NGC 5506 UV data with model 1 is not exact. Moreover, we have referred to the data in the UV for all galaxies considering that the flux drops at $\log \nu > 15.4$. A better fit to NGC 5506 can be obtained either by a power-law (pl) dominated model with $V_s = 200 \text{ km s}^{-1}$, $n_0 = 50 \text{ cm}^{-3}$, $\log F_H = 9.3$, $D = 6 \cdot 10^{17} \text{ cm}$, and $d/g = 5 \cdot 10^{-15}$ or with a black body (bb) dominated model with $V_s = 200 \text{ km s}^{-1}$, $n_0 = 200 \text{ cm}^{-3}$, $U = 0.01$, $T_* = 5 \cdot 10^4 \text{ K}$, $D = 5 \cdot 10^{16} \text{ cm}$, and $d/g = 10^{-14}$. In Fig. 3d, the contributions of these models to the continuum are represented by the long dash lines (thick) and the dash-dot lines (thick), respectively. The sum of the models will give an even better fit to the data. The data in the X-ray range are fitted by a model with $V_s = 900 \text{ km s}^{-1}$, $n_0 = 1000 \text{ cm}^{-3}$, $D = 8 \cdot 10^{17} \text{ cm}$, $d/g = 5 \cdot 10^{-13}$.

The bb model which fits the high frequency data represents the case where the bb flux from the stars reaches the very shock front of the clouds moving outwards from the AC. In other words, the dominant starbursts are located in the circumnuclear region.

Comparison of black – body and power – law dominated models

To distinguish starbursts from AGN we have run two models with shock parameters as model 5 and model 1, but with black body radiation with $T_* = 5 \cdot 10^4$ K (U=1), corresponding to a starburst and $T_* = 2 \cdot 10^5$ K (U=10), corresponding to a "warmer" (Terlevich & Melnick 1985), respectively. The results are presented for NGC 3081 (Figure 3b). For models with $V_s = 200$ km s^{-1} the shock prevails and there is no great difference between the pl model and the bb model. Diffuse radiation from the hot slabs of the gas downstream maintains the temperature of the gas at $\sim 1-2 \cdot 10^4$ K. On the other hand, in case of a low velocity shock ($V_s = 100 \text{ km s}^{-1}$), even a strong bb radiation flux corresponding to a high temperature cannot heat the gas enough to shift the peak in the optical-UV to $\log(\nu) > 15$ (see §2.1).

The contribution of an intermediate stellar population

It is suggested by Heckman et al (1995) that the optical-UV SED of the continuum can be fitted by the black body radiation from relatively high temperature stars. In fact, a young stellar population is observed in some galaxies, e.g. Mrk 477 (see Heckman et al. 1997). In Figure 4 we present the fit of the Mrk 477 continuum by black body fluxes corresponding to different temperatures. The three bumps correspond to $T_* = 4,000$ K (dash-dot line), $10,000$ K (long-dash line), and $20,000$ K (short-dash line). The second and the third one correspond to intermediate population stars (B). The ratios of the weights adopted to fit the data are $\text{bb}(4,000) : \text{bb}(10,000) : \text{bb}(20,000) = 3.2 \cdot 10^{-11} : 5 \cdot 10^{-23} : 1.6 \cdot 10^{-24}$. These are not able to explain the observational evidence of starburst activity (T. Contini 1999, private communication). Moreover, we assume that the UV emission by a younger ($T > 5 \cdot 10^4$ K) star population is absorbed by the clouds and reemitted as bremsstrahlung (see for example Figure 3b). So, we conclude that although intermediate population stars contribute to the continuum, the bremsstrahlung from illuminated clouds prevails. This is also consistent with the results of line spectra calculations.

2.3. The spectral slopes

One of the important observational features of optical-UV spectra in Seyfert 2 galaxies is the continuum slopes (Heckman et al. 1995). These suggest that the featureless continuum comes

from a reddened starburst in the ranges 1200 - 2600 Å ($F_\lambda \propto \lambda^\beta$) and 1910 - 4250 Å ($F_\lambda \propto \lambda^\gamma$). The frequencies corresponding to these critical wavelengths are indicated in Figure 3 by vertical lines.

In Table 3 the spectral slopes γ and β obtained from the models fitting each galaxy in the sample are compared with the values given by Heckman et al. (1995, Table 1).

The agreement is quite good, since our results depend on the fitting of the whole continuum spectra. It can be improved if more observational data become available in the different wavelength ranges. In particular, for NGC 2110 and MRK 34, a better agreement will probably be reached when data in the UV become available. Interestingly, the data in the different wavelengths correspond to different models. Table 3 shows that low γ values are provided by data which correspond to a model with relatively low V_s , low n_0 and $\log F_H = 12.7$ (models 1 and 2).

One important point regarding the slopes is the position of the optical-UV peak. This is highly dependent on the temperature across the cloud as shown in §2.1. The model dependence of the frequency corresponding to the peak position is illustrated in Figure 5, where the results for various models are plotted, with the curves shifted vertically for sake of clarity.

Another argument favoring the origin of the ultraviolet continuum of Seyfert 2 galaxies in a reddened population of hot stars is the correlation between the ratio of the infrared to the ultraviolet flux ($L_{\text{ir}}/L_{\text{uv}}$) and the slope of the ultraviolet continuum (Heckman et al. 1995). These follow the behavior of observed starbursts (Meurer et al. 1995). In Figure 6 we show the plot for the Seyfert 2 galaxies in the sample. For each galaxy, we plot the far-IR/UV ratio (see Table 1 of Heckman et al.) versus the two β values given in Table 3. The corresponding points are close, so the correlation is also present even if the continuum is not due to a reddened starburst but to the NLR emission.

Notice that dust emission is strongly coupled to gas emission (see, for instance, Viegas & Contini 1994) through shock and radiation effects and that L_{ir} also depends strongly on the dust-to-gas ratio. For both starburst and Seyfert galaxies the correlation shown in Figure 6 is usually used to show that the absorbed ultraviolet radiation is reemitted in the infrared. For Seyfert 2 galaxies, particularly, the relation between the central radiation source and infrared emission may not be direct, since both shocks and photoionization are powering the NLR, and, in our models, the observed UV continuum is not coming from the central source.

The results above indicate that the continuum emission from the NLR clouds may be another

explanation for the featureless continuum of Seyfert 2 galaxies. Since this component is extended, galaxies where this component is dominant should show little or no dilution of stellar absorption lines as discussed by Cid-Fernandes et al. (1998).

3. Constraining the models : the line spectra

In previous sections it was found that the SED of the continuum in the optical-UV range is mainly reprocessed radiation from heated gas clouds. Moreover, it was found that reradiation from clouds photoionized by black body radiation from young stars can hardly be distinguished from that from clouds photoionized by a power-law radiation flux. Three main cases are considered: 1) power-law radiation from the AC, 2) blackbody radiation from stars with $T_*=5 \cdot 10^4$ K which represent the starburst case, and 3) blackbody radiation from stars with $T_*=1-2 \cdot 10^5$ K which represents the Terlevich & Melnick (1985) case. So, the interpretation of the line spectra is essential for disentangling the domain of each mechanism.

Our suggestion that the featureless continuum in Seyfert 2 galaxies could be due to the NLR continuum emission can be tested by the observed emission lines. Our previous analysis of the Circinus galaxy and NGC 5252 showed that a self-consistent model can only be obtained by simultaneous fitting of the continuum and emission-line spectra (Contini et al 1998a, 1998b). Although a full discussion of the emission-line spectra is out of the scope of this paper, it is important to show that the models adopted to fit the continuum of the galaxies in the sample are also consistent with the observed line ratios.

Emission-line data for various objects were collected from the literature. Those for NGC 2110, NGC 2992, and NGC 5506 come from Shuder (1980); NGC 3081 comes from Durret & Bergeron (1986); NGC 3393 from Diaz, Prieto, & Wamsteker (1988); NGC 4388 from Pogge (1988); Mrk 3, Mrk 34, Mrk 78, Mrk 348, and Mrk 573 from Koski (1978); NGC 5135 and IC 5135 from Vaceli et al. (1997).

The emission-line intensity, relative to $H\beta$, for the most indicative lines in the optical range is listed in Table 4 for models 2, 3, 6, 9, 12 (Table 1). Models 2(SD) and 6(SD) correspond to models 2 and 6, respectively, but are calculated in the shock dominated (SD) case, i.e. adopting $F_H = 0$. The minimum and the maximum observed values for the galaxies referred to above are given in the second column, whereas model results appear in columns 3 to 9. Data for NGC 2110, which shows line ratios rather different than those of the other galaxies, are also included.

Various clouds of the NLR at different physical conditions must contribute to the continuum, as well as to the emission-line ratios. Therefore, multi-cloud model results obtained by averaged sums are also given in Table 4 (columns 10-12). The weights adopted in the averaged sums appear in the bottom of Table 4, as well as the calculated absolute values of $H\beta$ for the individual models. Notice that in order to have a good fit, the results of SD models are included. The weights of SD models are higher than those of radiation dominated models because the absolute fluxes are weaker (see Viegas et al. 1999). The averaged results are within the maximum and minimum observed ratios except for the [N I] emission-line, which is highly dependent on the geometrical depth. Concerning the [N II] 6584+ line, a slighter higher N/H abundance could provide better agreement (cf. Contini et al. 1999).

For sake of consistency, we present in Figure 7 the SEDs corresponding to the theoretical models AV1, AV2, and AV3. An hypothetical bb emission from the background old star population is also shown (long dash-dot lines) to better understand the diagrams. The SED maxima for shock-dominated models are determined by the shock velocity, whereas the optical-UV peaks in radiation-dominated models depend on the radiation flux. The model results are compared to the NGC 5643 data which are representative of the continuum shown by the galaxies in the sample. Notice that AV2 gives a better fit than AV1 and AV3, both in the near infrared and in the far ultraviolet. This suggests that the fit of the line spectra must include shock dominated models.

4. Concluding Remarks

The aim of this paper is to understand the continuum SED of Seyfert galaxies. We show that composite models for the NLR of Seyfert 2 galaxies can explain the full range of the observed continuum, and, in particular, the optical-ultraviolet continuum. Comparison of theoretical results and observational data shows that V_s of about $100-300 \text{ km s}^{-1}$, and n_0 of $200-300 \text{ cm}^{-3}$ must prevail in the NLR. Higher velocities may also be present in order to explain the soft X-ray emission.

Multi-cloud models are necessary to interpret the spectra (both line and continuum) of single objects, even in the global investigation of a sample of galaxies.

An important point is the characteristics of the featureless continuum of Seyfert 2 galaxies. Regarding the continuum slopes and the correlation between the far-infrared to ultraviolet ratio and the UV slope, both are reproduced by our models. This is an indication that the NLR

continuum emission may be the main components of featureless continuum.

The main result of our investigation is that the continuum observed in the HS sample is reprocessed radiation from the clouds of the NLR. These clouds are mainly powered by the central radiation, usually characterized by a power-law ionizing spectrum. Nevertheless, black body radiation from starbursts located in the outskirts of the nuclear region may, in some cases, contribute to the UV data. The results will be confirmed when further data in the far-UV become available.

Acknowledgements. We are grateful to the referee for enlightening comments and to G. Drukier for reading the manuscript. This paper is partially supported by the Brazilian financial agencies: FAPESP (1997/13816-4), CNPq (304077/77-1), and PRONEX/Finep(41.96.0908.00).

References

Aaronson,M. et al. 1981, MNRAS, 195, 1;

Allen, C.W. 1973 in "Astrophysical Quantities" (Athlon)

Allen,D.A. 1976, ApJ, 207, 367;

Becker,R.M., White,R.L., & Edwards, A.L. 1991, ApJS, 75, 1;

Boroson,T.A.,Strom,K.M., & Strom,S.E. 1983, ApJ, 274, 39;

Cid-Fernandee, R., Dottori, H., Gruenwald, R. & Viegas, S. M. 1991,
MNRAS 255, 165

Cid-Fernandes, R., Storchi-Bergmann, T. & Schmitt,H. 1998, MNRAS,
297, 579

Contini,M., Prieto,M.A., & Viegas,S.M. 1998a, ApJ, 492, 511

Contini,M., Prieto,M.A., & Viegas,S.M. 1998b, ApJ, 505, 621

Contini,M., Radovich,M., Rafanelli,P., & Richter,G. 1999, submitted

De Vaucouleurs, A. & Longo, G. 1988, Catalogue of Visual and Infrared
Photometry of Galaxies from 0.5 μ m to 10 μ m (1961-1985);

De Vaucouleurs, G. et al. 1991 Third Reference Catalogue of Bright
Galaxies,

Diaz,A.I., Prieto, M.A., & Wamsteker,W. 1988, A&A, 195, 53

Doroshenko,V.T. & Terebezh,V.Yu 1979, SvAL, 5, 305;

Drain,B.T., & Lee,H.M. 1994, ApJ, 285, 89

Durret,F. & Bergeron,J. 1986, A&A, 156, 51

Fabbiano,G., Kim, D.-W.,& Trinchieri, G. 1992, ApJS, 80, 531;

Frogel,J.F., Elias,J.H., & Phillips,M.M. 1982, ApJ, 260, 70;

Glass,I.S. 1973, MNRAS, 164, 155;

Glass,I.S. 1976, MNRAS, 175, 191;

Glass,I.S. 1978, MNRAS, 183, 85;

Glass,I.S. 1979, MNRAS, 186, 29;

Glass,I.S. 1981, MNRAS, 197, 1067;

Glass,I.S. et al. 1982, A&A, 107, 276;

Gower,J.F.R., Scott,,P.F., & Wills,D. 1967, MmRAS, 71, 49;

Gregory,P.C. & Condon,J.J. 1991, ApJS, 75, 1011;

Gregory,P.C. et al. 1994, ApJS, 90, 173;

Griersmith,D., Hyland, A.R., & Jones, T.J. 1982, AJ, 87, 1106;

Griffith,M.R. et al. 1994, ApJS, 90, 179;

Griffith, M.R. 1995, ApJS, 97, 347;

Heckman,T., Krolik,J., Meurer,G., Calzetti,D., Kinney,A., Koratkar,A., Leitherer,C., Robert,C., & Wilson,A. 1995, ApJ, 452, 549

Heckman,T.M. et al. 1997, ApJ, 482, 114

Joyce,R.R. & Simon, M. 1976, PASP, 88, 870;

Kinney,A.I. et al. 1993, ApJS, 86, 5;

Kormendy,J. 1977, ApJ, 214, 359;

Koski,A.T. 1978, 223, 56

Large,M.I. et al. 1981, MNRAS, 194, 693;

Lauberts,A. & Valentijn,E.A. 1989, The Surface Photometry Catalogue of the ESO-Uppsala Galaxies, 1989, Garching Bei Munchen ESO;

Leitherer,C., Robert,C., & Heckman, T. 1995 ApJS, 99, 173

Maddox,S.J. et al. 1990, MNRAS, 243, 692;

Mathewson,D.S. & Ford, V.L. 1996, ApJS, 107, 97;

McAlary,C.W.,McLaren,R.A., & Crabtree,D.R. 1979, ApJ, 234, 471;

McAlary,C.W. et al. 1983, ApJS, 52, 341;

Meurer, G., Heckman, T., Leitherer, C., Kinney, A., Robert, C., & Garnett, D. 1995, AJ, 110, 2665

Moshir, M. et al. 1990, Infrared Astronomical Satellite Catalogs, 1990, The Faint Source Catalog, Version 2.0;

Mould,J.,Aaronson,M.,& Huchra,J. 1988, ApJ, 238, 458;

Neugebauer,G. et al. 1976, ApJ, 205, 29;

Pogge,R.W. 1988, ApJ, 332, 702

Rieke,G.H. 1978, ApJ, 226, 550;

Rieke,G.H. & Low,F.J. 1972, ApJ, 176L, 95;

Rudy,R.J.,Levan,P.D., & Rodriguez-Espinosa,J.M. 1982

Sandage,A. & Visvanathan,N., 1978, 223,707;

Scoville,N.Z. et al. 1983, ApJ, 271, 512;

Shuder,J.M. 1980, ApJ 240, 32

Soifer,B.T. et al. 1989, AJ, 98, 766;

Stein,W.A. & Weedman,D.W. 1976, 205, 44;

Terlevich, R. & Melnick, J. 1985, MNRAS, 213, 841

Tran, H. D. 1995, ApJ, 440, 578

Vaceli,M.S., Viegas,S.M., Gruenwald,R., & De Souza,R.E. 1997, AJ, 114, 1245

Viegas,S.M. & Contini,M. 1994, ApJ, 428, 113

Viegas,S.M., Contini,M., & Contini,T. 1999, A&A, 347, 112

Wang,T. et al. 1999, ApJ, 515, 567

Ward,M. et al. 1982, MNRAS, 199, 953;

Weaver,K.A. et al. 1995, ApJ, 442, 597

White,R.L. & Becker,R.H. 1992, ApJS, 79, 331;

Wright,A.E. et al 1996, ApJS, 103, 145;

Wright,A.E. et al. 1994, ApJS, 91, 111;

Wright,A. & Otrupcek,R. 1990, Parkes Catalogue, 1990, Australia
Telescope National Facility;

Xue,S.-J. et al. 1998, PASJ, 50, 519

Figure Captions

Fig. 1

The results corresponding to a power-law ionizing radiation (a) and a $5 \cdot 10^4$ K blackbody radiation (b). In each figure, the left panel show the temperature distribution across a cloud, where the left edge of the diagram corresponds to the shock front, while the right edge to the photoionized side. The thin vertical line in the middle of the diagrams indicates the separation of the cloud in two halves. The axis scales are logarithmic. The horizontal axis scale is symmetric in order to provide an equal view of the two sides of the cloud, that dominated by collisional ionization and the radiation dominated one. The right panel shows the corresponding spectral energy distribution. The power-law results refer to $V_s = 100 \text{ km s}^{-1}$ and $n_0 = 100 \text{ cm}^{-3}$ (thin lines) and to $V_s = 300 \text{ km s}^{-1}$ and $n_0 = 300 \text{ cm}^{-3}$ (thick lines). Solid, short-dashed, and long-dashed lines correspond to $\log F_H = 12, 11, \text{ and } 10$, respectively. The black body results were obtained for $U = 0.01$ (long-dashed), 0.1 (short-dashed), and 1. (solid), and $U = 100$. (dash-dot line).

Fig. 2

The spectral luminosities of all the galaxies of the Heckman et al. (1995) sample.

Fig. 3

The fit of the calculated to the observed SED for all the objects of the Heckman et al. sample. Solid lines : models 4, 11, 12, and 13; short dashed lines : models 5, 6, and 7 ; long dashed lines : models 1, 2; short dash-dot lines : models 3 and 8; dotted lines : models 14, 15 and 16; long dash-dot : the black body emission from the background old star population. Filled squares represent the data. Vertical thin lines define the crucial wavelengths at 4250 Å, 2600 Å, 1910 Å, and 1200 Å (see §2.3).

Fig. 4

The fit of MRK 477 continuum SED by star population at different temperatures. The three bumps between $14 < \log(\nu) < 15$ correspond to black body radiation with $T_* = 4,000 \text{ K}$ (dash-dot line), $10,000 \text{ K}$ (long-dash line), and $20,000 \text{ K}$ (short-dash line). Solid lines correspond to bremsstrahlung emission from the gas

and to IR thermal emission from dust from the NLR clouds (see Figure 3i).

Fig. 5

Comparison of the optical-UV peaks in the SED of the continuum calculated by models presented in Figs. 1a and 1b. 1 : $V_s=100 \text{ km s}^{-1}$, $n_0= 100 \text{ cm}^{-3}$, $\log F_H=12$; 2 : $V_s=100 \text{ km s}^{-1}$, $n_0= 100 \text{ cm}^{-3}$, $\log F_H=11$; 3 : $V_s=300 \text{ km s}^{-1}$, $n_0= 300 \text{ cm}^{-3}$, $\log F_H=12$; 4 : $V_s=300 \text{ km s}^{-1}$, $n_0= 300 \text{ cm}^{-3}$, $U=1$; 5 : $V_s=300 \text{ km s}^{-1}$, $n_0= 300 \text{ cm}^{-3}$, $U=0.1$; 6 : $V_s=300 \text{ km s}^{-1}$, $n_0= 300 \text{ cm}^{-3}$, $U=0.01$; 7 : $V_s=100 \text{ km s}^{-1}$, $n_0= 100 \text{ cm}^{-3}$, $U=1$; 8 : $V_s=100 \text{ km s}^{-1}$, $n_0= 100 \text{ cm}^{-3}$, $U=0.1$; 9 : $V_s=500 \text{ km s}^{-1}$, $n_0= 500 \text{ cm}^{-3}$, $U=1$;

Fig. 6

The far-infrared to ultraviolet luminosity ratio ($L_{\text{ir}}/L_{\text{uv}}$) versus the slope of the ultraviolet continuum β (see §2.3). The circles refer to our results and the stars to Heckman et al. (1995), as listed in Table 3. The straight line represents the correlation obtained from starburst data (Meurer et al. 1995).

Fig. 7

The SED of the continua referring to the multi-cloud models AV1, AV2, and AV3 (Tables 4). Shock dominated models are represented by dotted lines, model 3 by short dash-dot, model 6 by long dash, and model 12 by solid lines. Model 2 has a low weight and does not appear in the figures. An hypothetical bb emission from the background old star population is also shown (long dash-dot lines). Filled squares refer to NGC 5643 data.

Table 1
Input parameters for the models

model	n_0	V_s	$\log(F_H^o)$	D	d/g
(1)	(2)	(3)	(4)	(5)	(6)
1	150	100	12.7	3(16)	5(-15)
2	150	100	12.7	3(16)	3(-14)
3	400	100	(1.5,5.0)*	3(16)	5(-15)
4	400	150	12	3(16)	5(-17)
5	200	200	11.7	3(18)	5(-16)
6	200	200	11	3(18)	1(-15)
7	200	200	11	3(19)	7(-16)
8	200	200	(0.1,5.3)*	4.5(17)	5(-15)
9	200	200	(1.,4.7)*	3(18)	1(-15)
10	200	200	(0.01,4.7)*	5(16)	1(-14)
11	200	300	12	3(18)	5(-15)
12	200	300	12	3(18)	1(-13)
13	100	400	12	5.5(18)	5(-13)
14	200	900	SD	8(17)	5(-13)
15	1000	1000	SD	3(18)	2(-14)
16	1000	1000	SD	3(18)	5(-15)

$^o U = F_H / (nc(\alpha-1)) ((E_H)^{-\alpha+1} - (E_c)^{-\alpha+1})$

(E_c = high energy cutoff = 3000 eV, E_H =ionization potential of H.

* Blackbody radiation characterized by $(U, \log(T_*))$

Table 2a
The references of the continuum data

galaxy	references
NGC 2110	1, 2, 3, 4, 5
NGC 2992	1, 2, 3, 6, 7, 8, 9, 10
NGC 3081	3, 6, 7, 11, 12, 13, 14
NGC 3393	4, 7, 10, 11, 12
NGC 4388	4, 6, 7, 11, 15, 16, 17, 18, 19, 20, 21
NGC 5135	4, 6, 7, 11, 12, 22
NGC 5506	1, 2, 3, 4, 6, 7, 8, 11, 19, 24, 25
NGC 5643	4, 6, 7, 11, 12, 15, 26, 27
NGC 5728	4, 6, 7, 11, 19, 28
NGC 6221	1, 7, 9, 11, 12, 15, 26, 27
NGC 7582	1, 2, 4, 6, 7, 8, 9, 11, 12, 15, 27, 29, 30, 31, 32, 33, 34, 35
MRK 3	4, 7, 15, 20, 21, 28, 36, 37, 38, 39
MRK 34	4, 36, 37, 40
MRK 78	4, 36
MRK 348	4, 7, 11, 15, 20, 21, 25, 36, 38, 45
MRK 463	4, 7, 11, 20, 21, 41, 42
MRK 477	4, 7, 11, 43, 44
MRK 573	4, 7,
IC 3639	3, 4, 7, 11, 12
IC 5135	4, 7, 11, 12

1:McAlary et al. 1983; 2:Glass 1981; 3:Ward et al. 1982; 4:Moshir et al. 1990; 5:Griffith 1995; 6:Fabbiano, Kim, & Trinchieri 1992; 7:De Vaucouleurs et al. 1991; 8:Glass 1979; 9:Glass et al. 1982; 10:Griffith et al. 1994; 11:Kinney et al. 1993; 12:Lauberts & Valentijn 1989; 13:Kormendy 1977;

Table 2b

The best fitting models

galaxy	T_{old}	n_0	V_s	$\log(F_H)$	D	d/g	$\log(W)$	η
(1)	(2)	(3)	(4)	(5)	(6)	(7)	(8)	(9)
NGC 2110	3000	-	-	-	-	-	-18.9	-
		150	100	12.7	3(16)	3(-14)	-12.1	-
		200	200	11.7	3(18)	5(-16)	-10.35	0.088
		200	300	12	3(18)	1(-13)	-11.3	-
NGC 2992	4000	-	-	-	-	-	-19.1	-
		200	200	11.7	3(18)	5(-16)	-10.5	0.07
		1000	1000	s.d.	3(18)	2(-14)	-12.9	-
NGC 3081	4000	-	-	-	-	-	-19.3	-
		150	100	12.7	3(16)	3(-14)	-11.2	-
		150	100	(10,5.3)	3(16)	3(-14)	-9.2	-
		200	200	11.7	3(18)	5(-16)	-10.6	0.06
		200	200	(1.,4.7)	3(18)	5(-16)	-10.6	-
NGC 3393	4000	-	-	-	-	-	-20.35	-
		200	200	(0.1,5.3)	4.5(17)	5(-15)	-11.1	-
		200	200	11	3(19)	7(-16)	-10.7	0.115
		100	400	12	5.5(18)	5(-13)	-12.7	-
		200	900	s.d.	8(17)	5(-13)	-12.4	-
NGC 4388	4000	-	-	-	-	-	-18.5	-
		150	100	12.7	3(16)	5(-15)	-10.95	-
		200	200	11.7	3(18)	5(-16)	-9.7	0.52
		1000	1000	s.d.	3(18)	2(-14)	-14.4	-
NGC 5135	4000	-	-	-	-	-	-19.	-
		150	100	12.7	3(16)	3(-14)	-10.75	-
		200	200	11	3(18)	1(-15)	-9.1	1.
		1000	1000	s.d.	3(18)	2(-14)	-14.7	-
NGC 5506	3000	-	-	-	-	-	-18.4	-
		200	50	9.3	6(17)	5(-15)	-8.	-
		200	200	11	3(18)	1(-15)	-10.	0.14
		200	200	(0.01,4.7)	5(16)	1(-14)	-8.	-
		200	300	12	3(18)	1(-13)	-10.8	-
NGC 5643	4000	-	-	-	-	-	-18.5	-
		150	100	12.7	3(16)	5(-15)	-11.3	-
		150	100	12.7	3(16)	3(-14)	-11.4	0.003
		200	200	11	3(18)	1(-15)	-9.3	0.3
		1000	1000	s.d.	3(18)	2(-14)	-13.3	-
NGC 5728	5000	-	-	-	-	-	-19.5	-
		150	100	12.7	3(16)	3(-14)	-11.2	-
		200	200	11	3(18)	1(-15)	-10.4	0.13
		1000	1000	s.d.	3(18)	2(-14)	-14.6	-
NGC 6221	5000	-	-	-	-	-	-19.0	-
		150	100	12.7	3(16)	5(-15)	-11.4	-
		200	200	11.7	3(18)	5(-16)	-10.0	0.09
		1000	1000	s.d.	3(18)	5(-15)	-13.2	-
MRK 3	4000	-	-	-	-	-	-19.6	-
		200	300	12	3(18)	1(-13)	-10.8	0.11
MRK 34	4000	-	-	-	-	-	-20.2	-
		200	300	12	3(18)	1(-13)	-11.5	0.3

Table 3
The γ and β indices

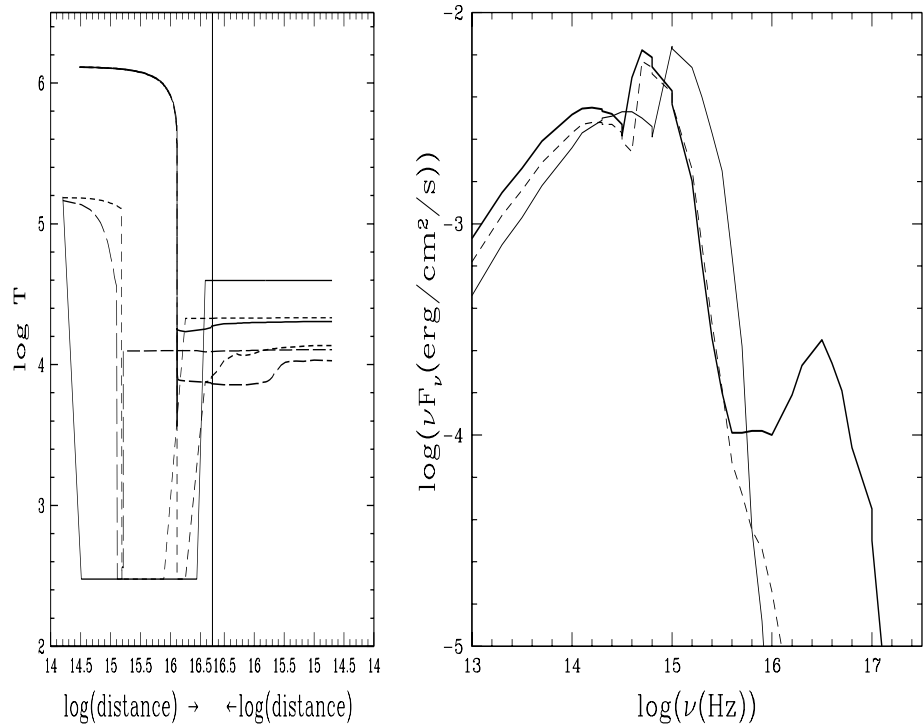
galaxy	γ (HS)	γ (mod)	β (HS)	β (mod)
(1)	(2)	(3)	(4)	(5)
NGC 2110	0.7	1.3*	-	-
NGC 2992	1.0	1.16	-	-
NGC 3081	1.2	0.4	-0.4	-0.5
NGC 3393	1.5	1.88	-0.4	-0.7
NGC 4388	1.0	1.0	-0.9	-0.6
NGC 5135	0.4	0.5	-0.1	-0.1
NGC 5506	0.9	1.16	-0.4	-0.7
NGC 5643	2.	1.6	-0.3	-0.5
NGC 5728	1.4	1.0	-0.6	-0.4
NGC 6221	1.0	1.59	0.4	0.49
NGC 7582	2.5	2.5	1.7	1.38
MRK 3	1.6	1.88	-0.3	-
MRK 34	0.6	1.59*	-0.6	-
MRK 78	1.4	1.8	0.0	-
MRK 348	0.2	0.58	0.1	0.19
MRK 463	-0.2	-0.42	-0.7	-0.4
MRK 477	-0.6	-0.3	-1.3	-1.0
MRK 573	0.9	1.3	-0.7	-
IC 3639	0.3	0.2	-1.0	-1.7
IC 5135	0.9	0.43	-0.5	-0.43

* UV data are not available

Table 4
The average emission-line spectra

emission-line	obs	2(SD)	6(SD)	2	3	6	9	12	AV1	AV2	AV3
(1)	(2)	(3)	(4)	(5)	(6)	(7)	(8)	(9)	(10)	(11)	(12)
[OII] 3727	1.9-6.4	72.	40.	0.	5(-4)	1.2	1.6	0.04	6.35	2.0	3.36
[NeIII] 3869	0.7-2.3	3.0	3.3	4(-4)	0.3	0.66	0.68	1.0	0.92	0.7	0.98
[OIII] 4363	0.13-0.35	2.25	2.0	1(-4)	0.03	0.05	0.04	0.1	0.29	0.1	0.21
HeII 4686	0.06-0.48	0.02	0.1	1.0	1.1	0.086	0.027	0.5	0.41	0.44	0.49
[OIII] 5007+	6.4-16.0	28.2	24.8	0.01	1.9	10.	9.8	18.	11.1	9.7	15.
[NI] 5200	0.07-0.24	0.16	0.09	0.0	0.0	0.020	0.028	0.0	0.02	0.013	0.01
HeI 5876	0.05-0.19	0.15	0.2	0.0	0.001	0.13	0.19	0.08	0.1	0.085	0.08
[FeVII] 6086	0.01-0.19	0.003	0.003	0.0	0.61	5(-4)	1(-3)	1(-5)	0.15	0.17	0.09
[OI] 6300+	0.3-1.6	0.46	0.5	0.0	0.0	0.87	1.12	1(-5)	0.46	0.46	0.18
[NII] 6584+	2.0-6.1	8.6	6.8	0.0	3(-4)	2.50	3.90	0.018	2.0	1.5	0.9
[SII] 6717	0.7-1.6	2.3	1.28	0.0	0.0	1.24	1.54	0.6	0.86	0.8	0.68
[SII] 6731	0.1-1.6	2.5	1.96	0.0	0.0	1.78	2.00	1.2	1.27	1.2	1.17
H β (erg cm $^{-2}$ s $^{-1}$)	-	7.(-5)	2.2(-4)	1.8(-3)	0.67	0.75	0.38	13.5	-	-	-
W(AV1)	-	4000	3000	0.1	3.0	5.0	-	0.1	-	-	-
W(AV2)	-	2000	10	0.1	3.0	5.0	-	0.1	-	-	-
W(AV3)	-	1000	1000	0.1	1.0	1.0	-	0.2	-	-	-

Fig. 1a



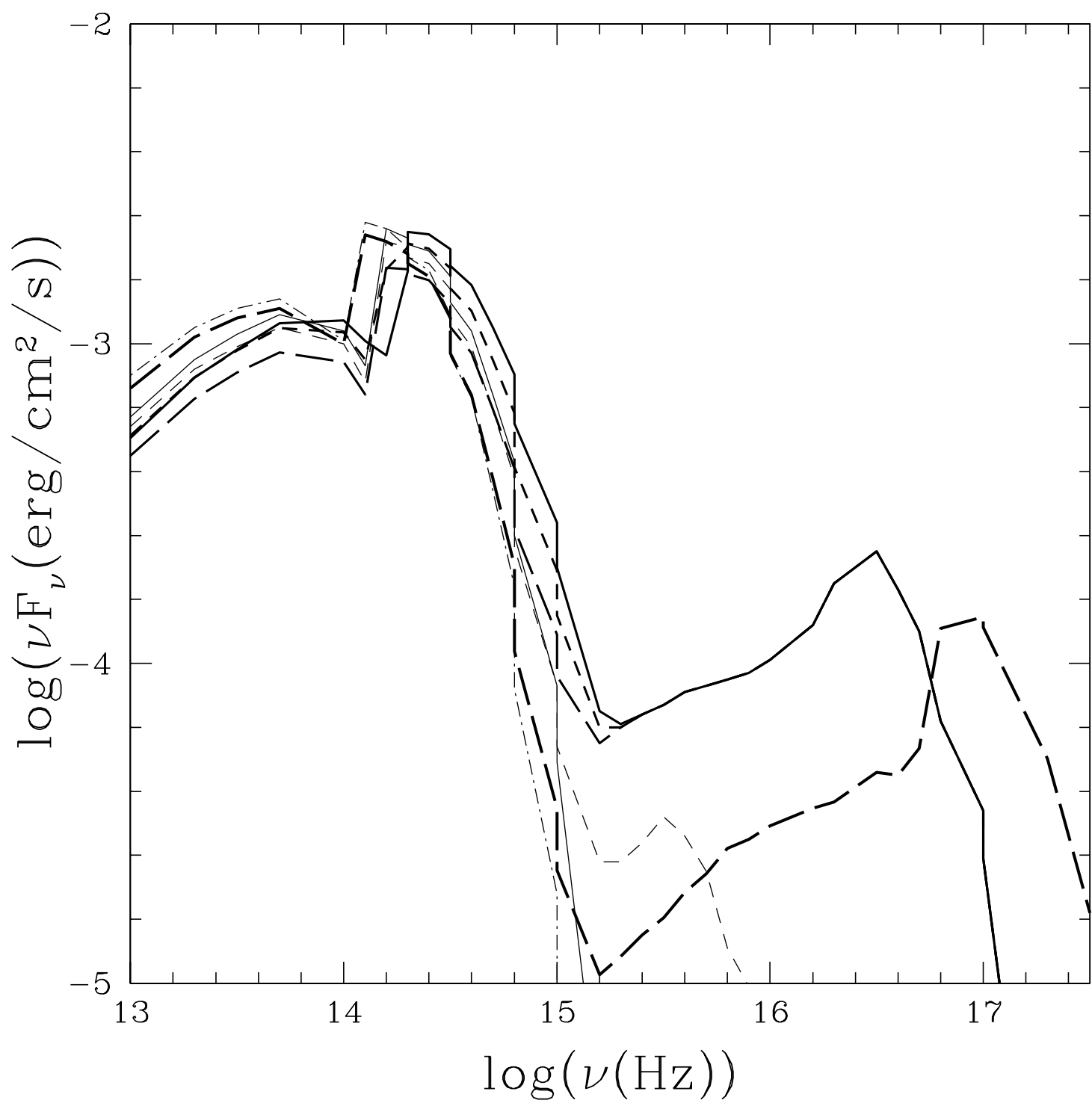


Fig. 3b

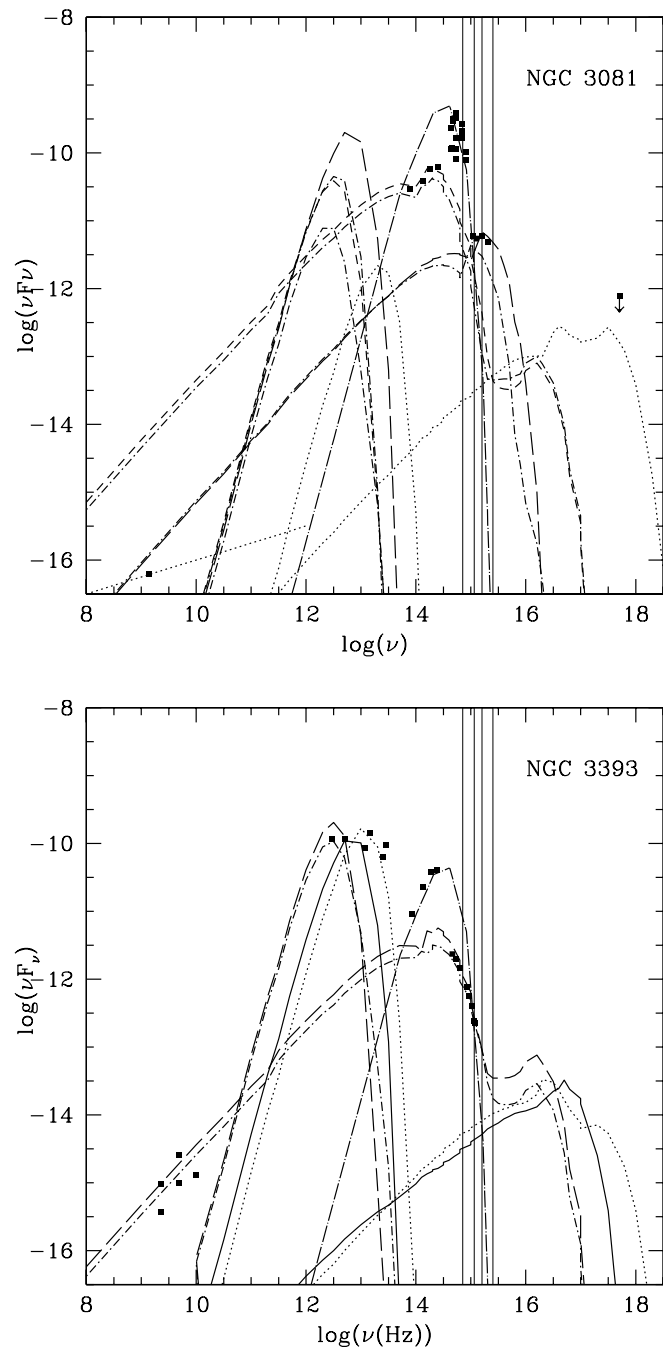


Fig. 3c

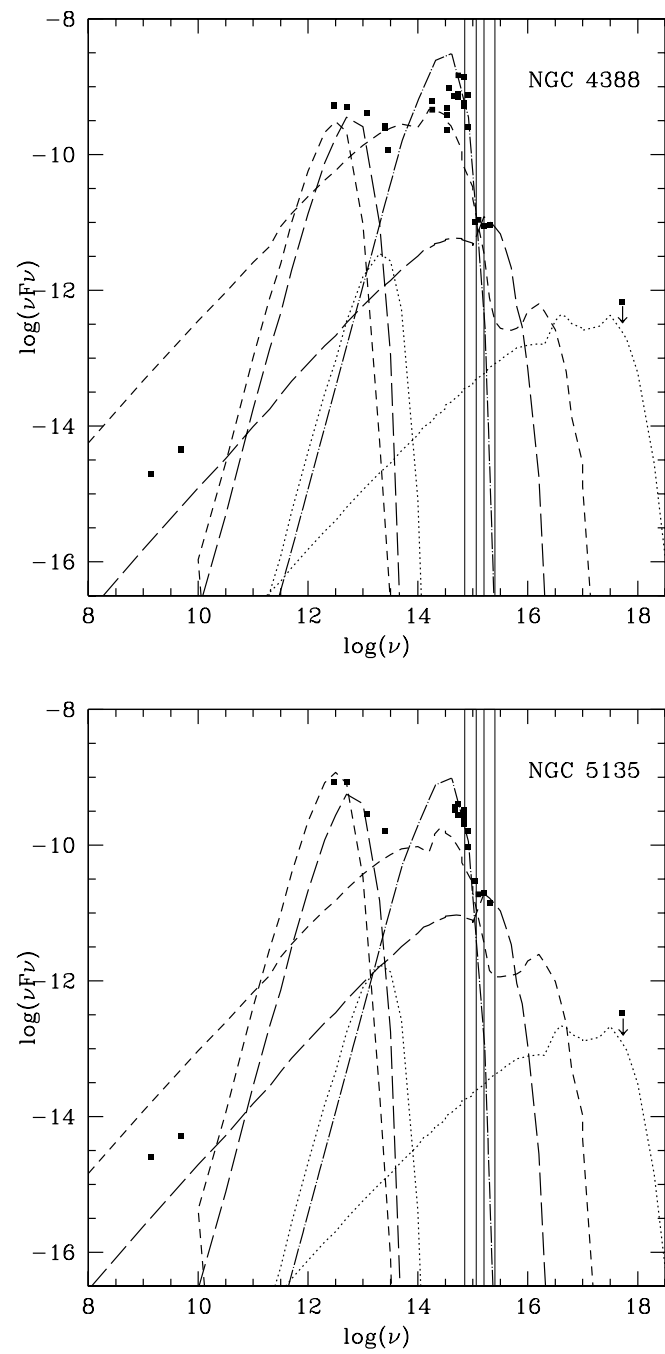


Fig. 3d

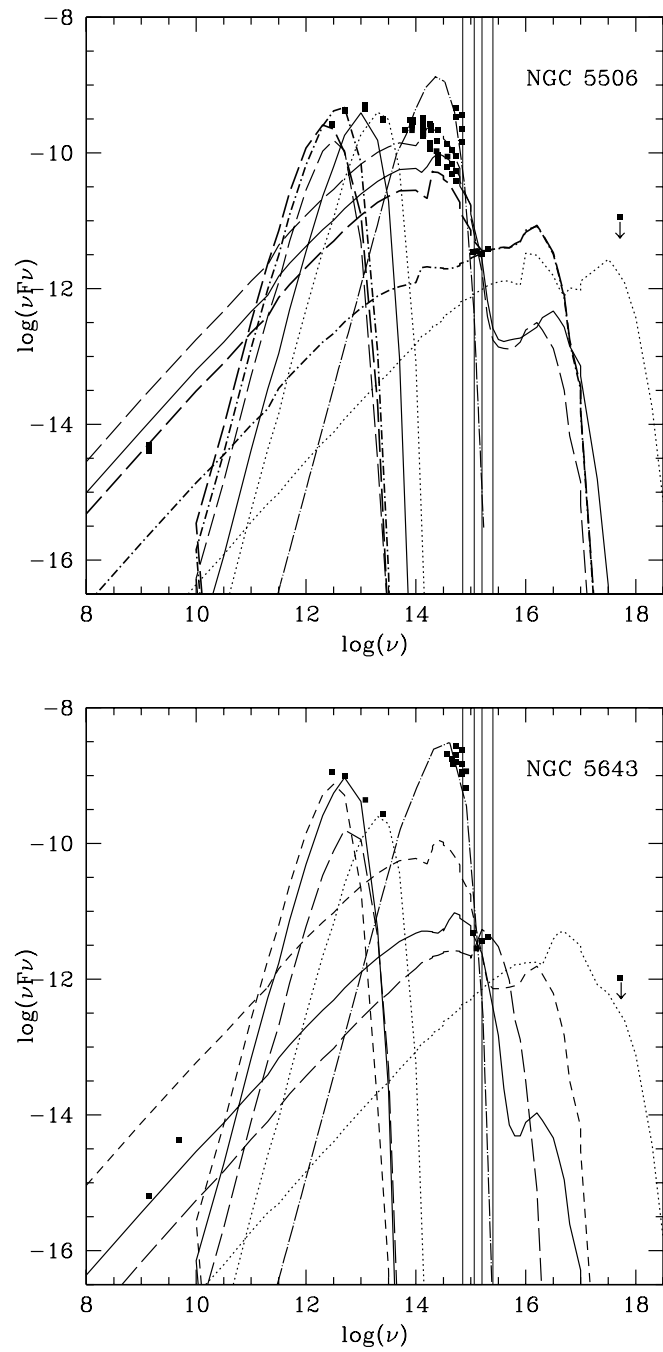


Fig. 3f

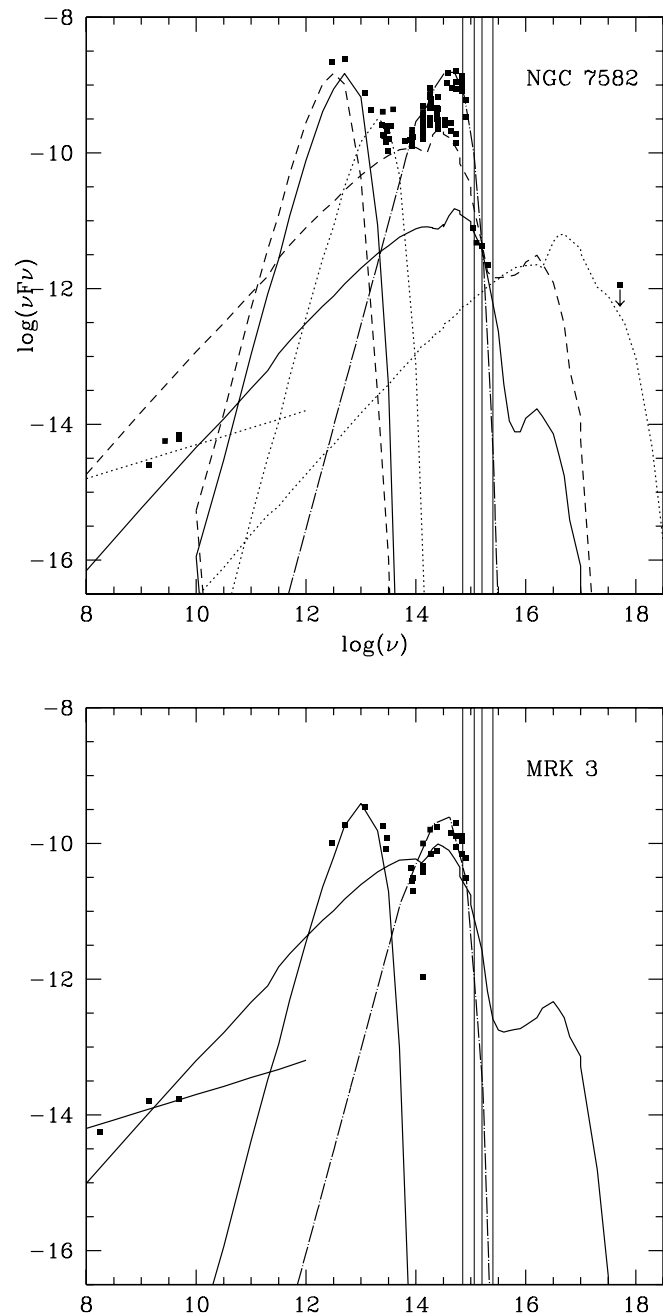


Fig. 3g

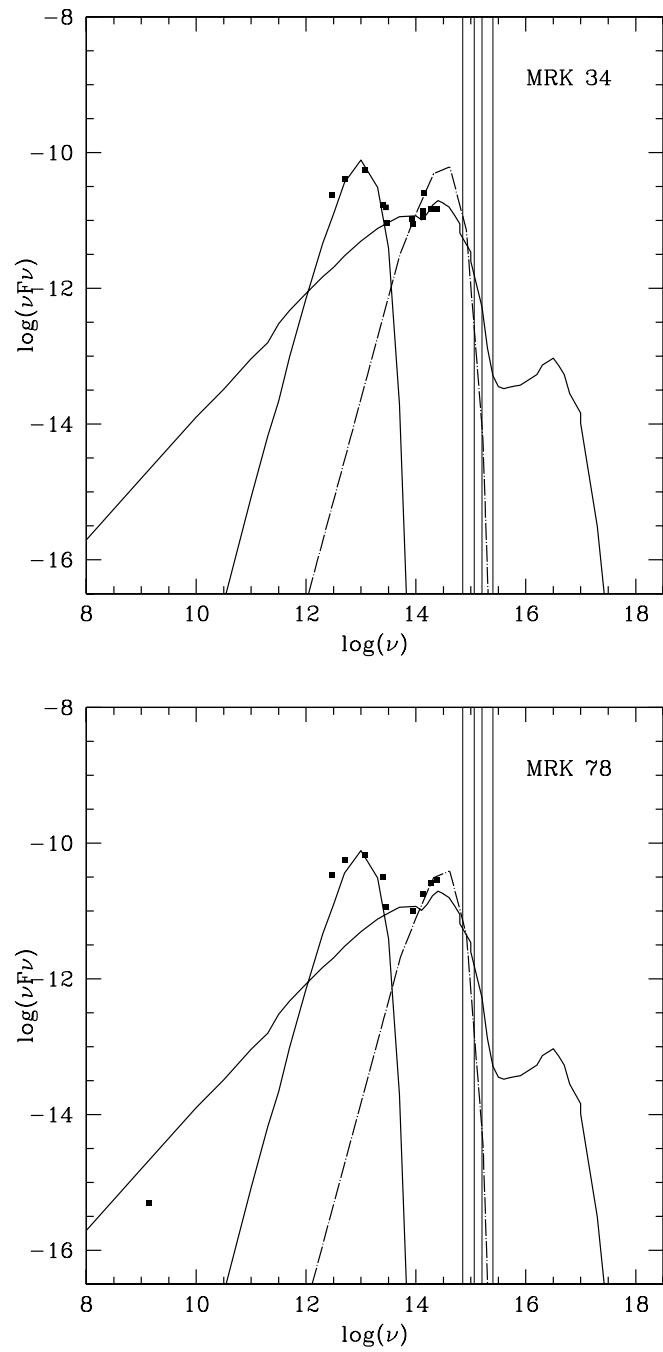


Fig. 3h

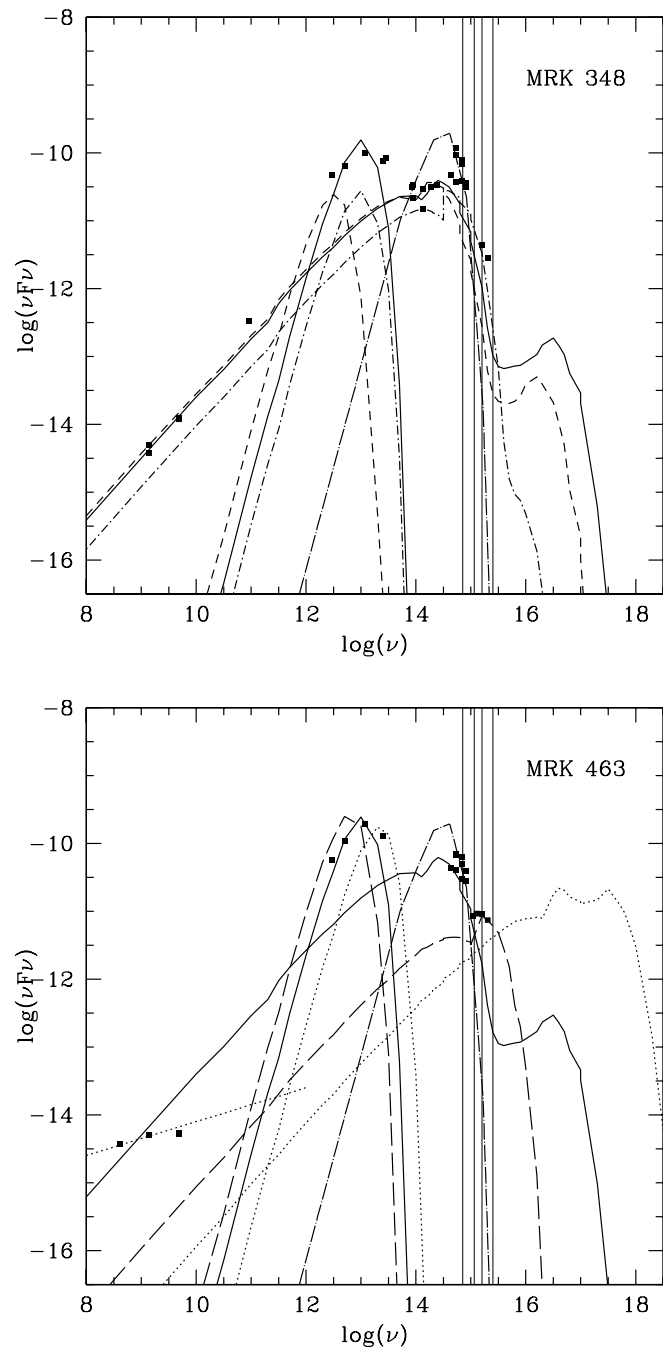


Fig. 3i

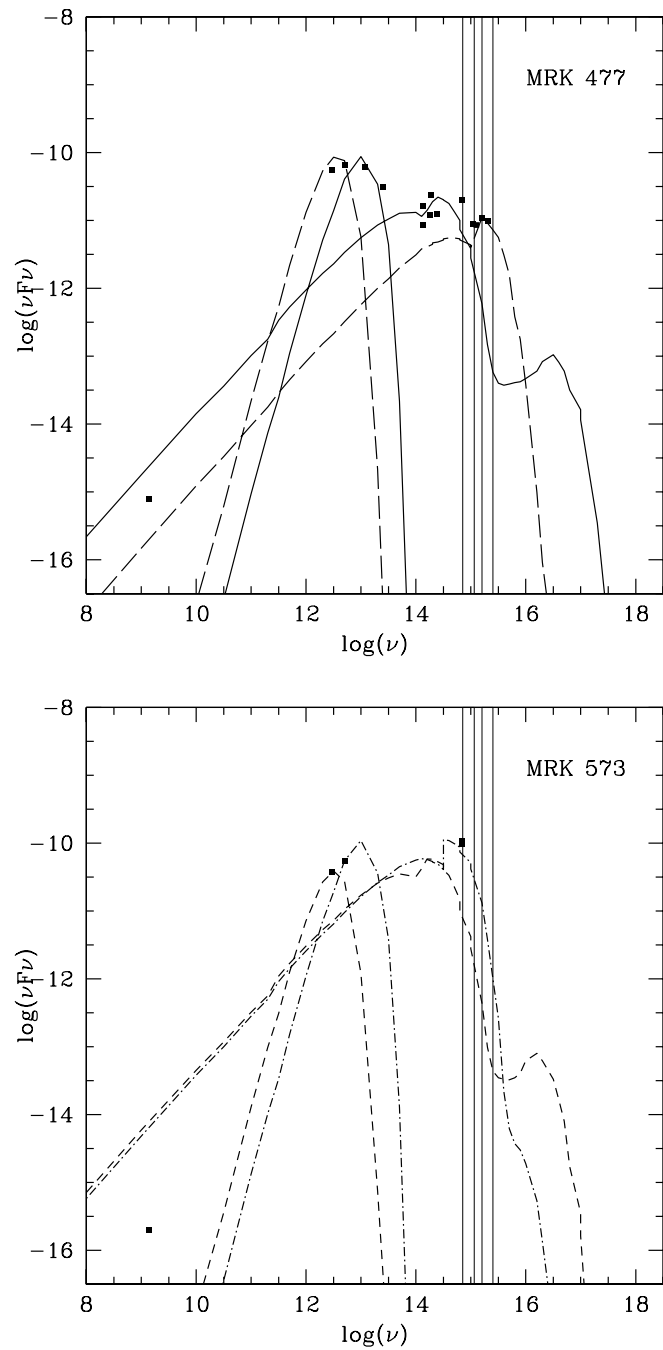
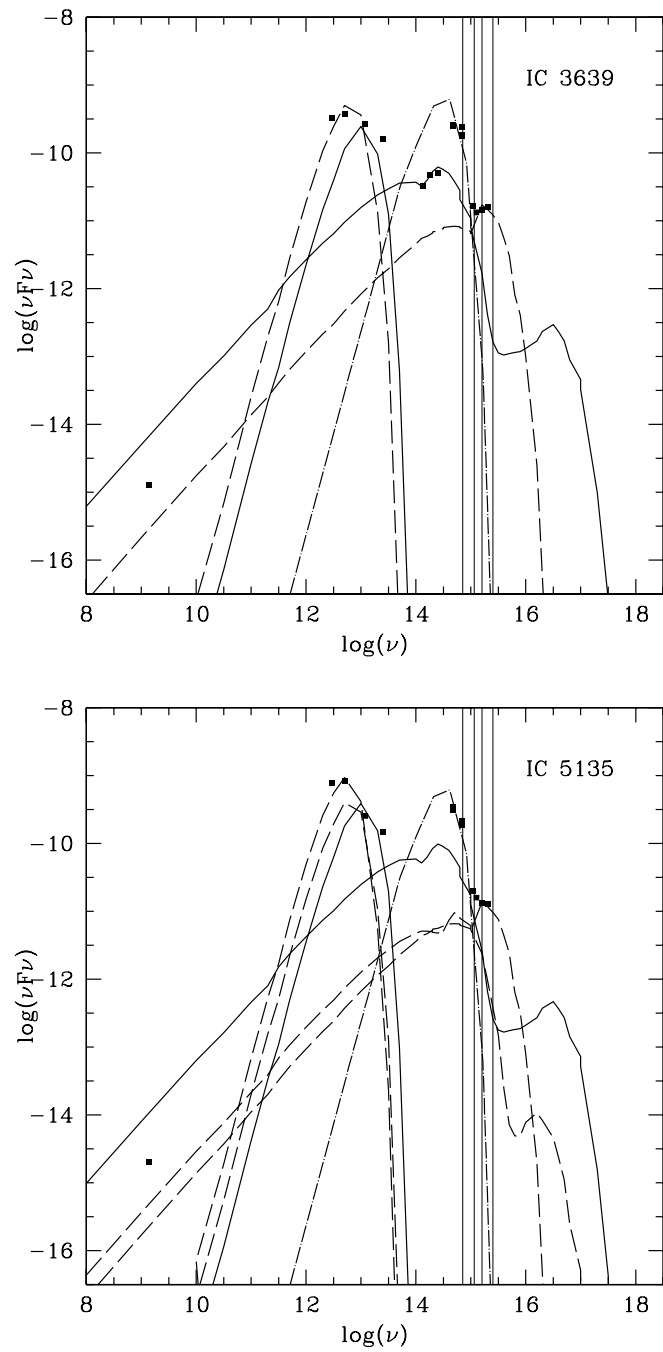
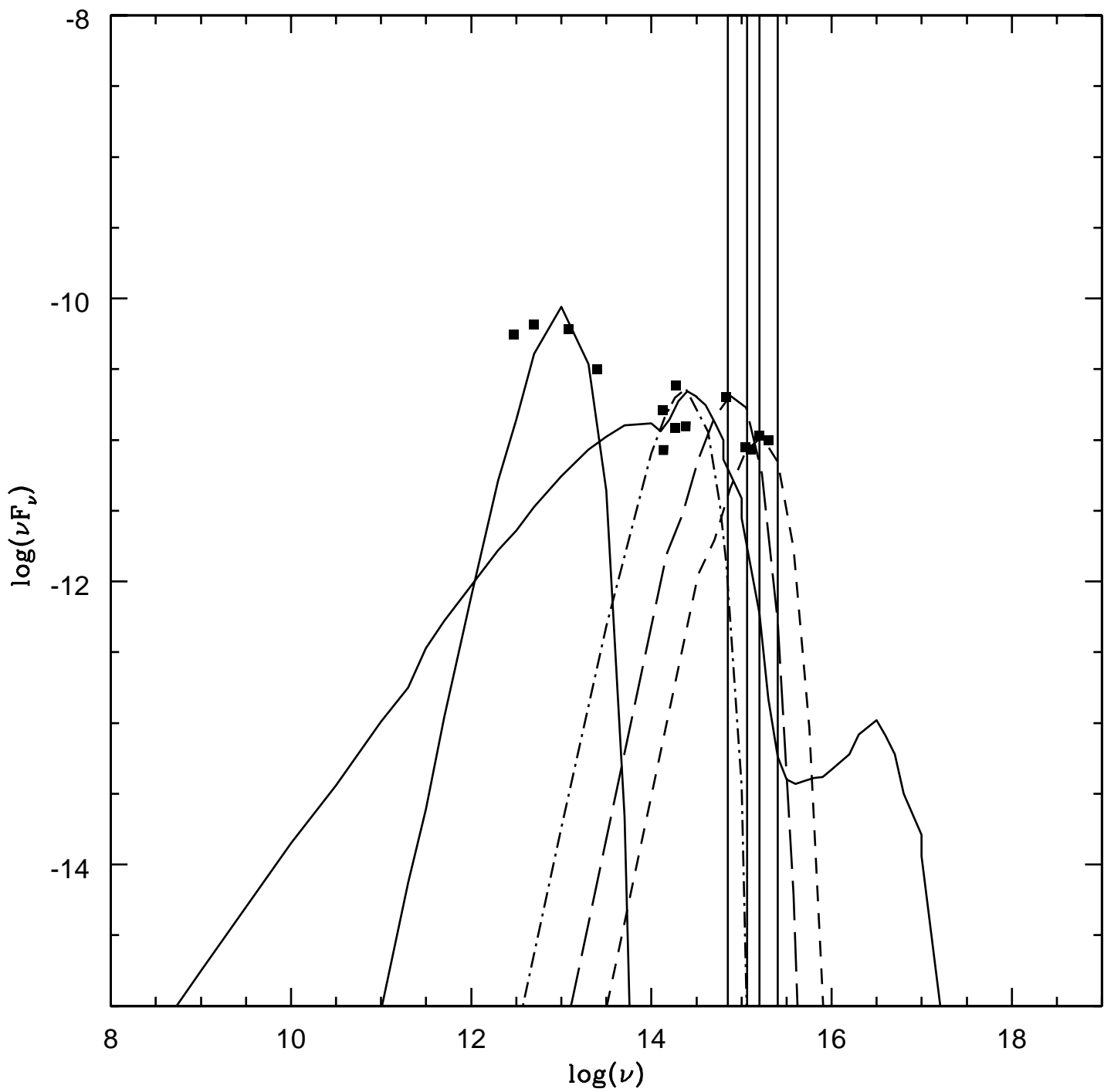
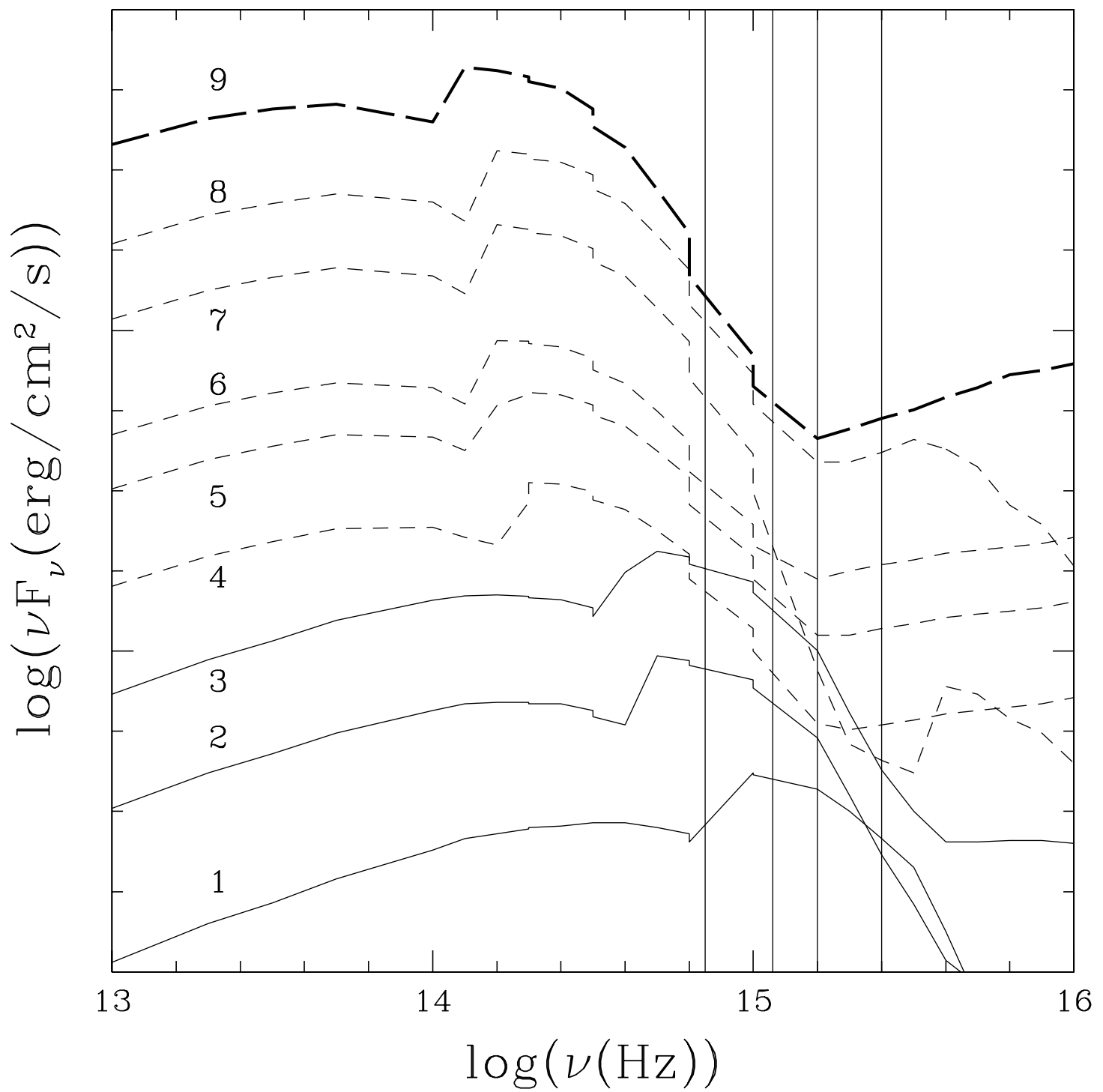


Fig. 3l







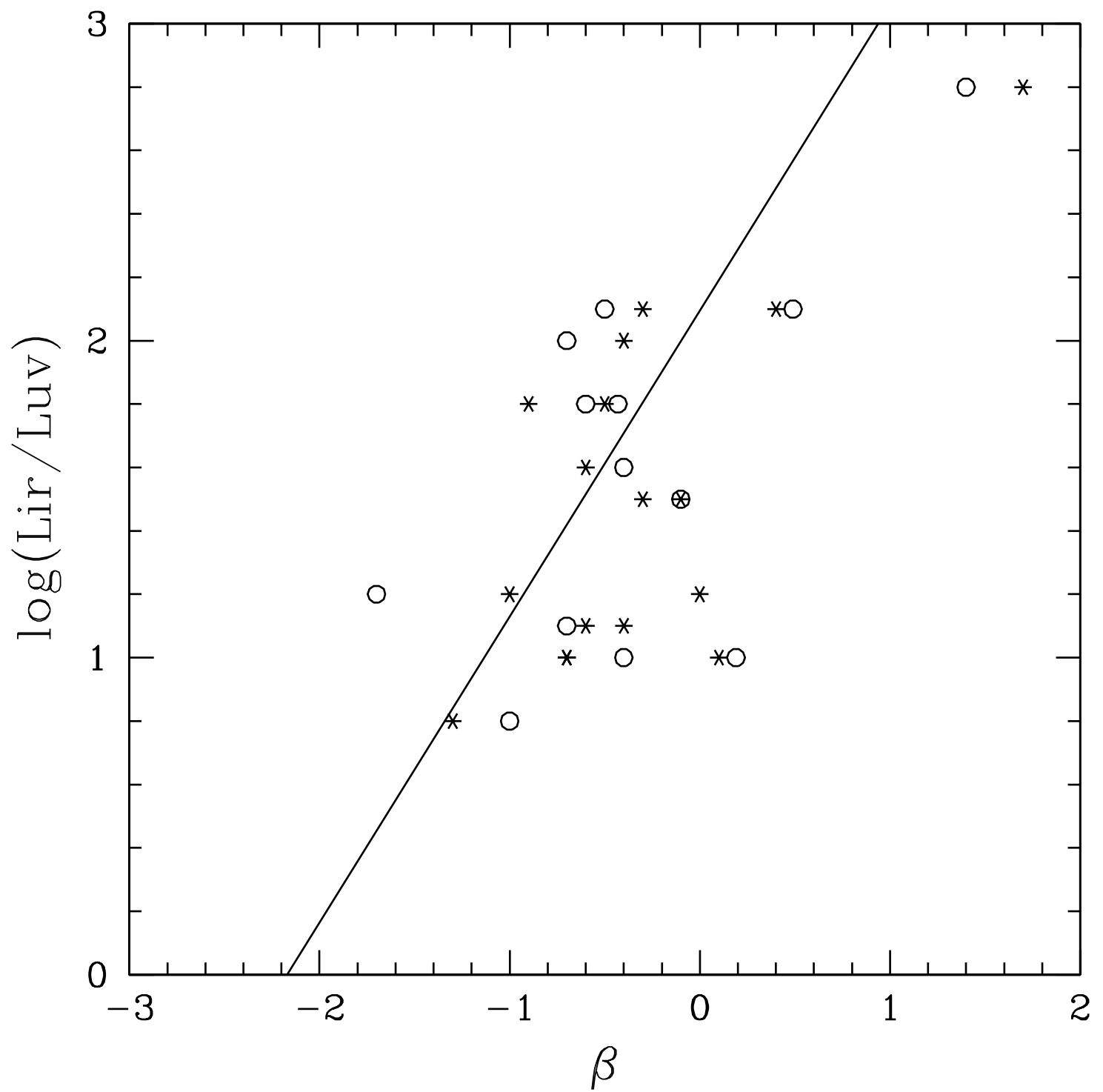


Fig. 7

